LAF | https://doi.org/10.15302/J-LAF-2026-0046
Volume 14 / Issue 6 / 260046 / 2026
Received Date | 2025-09-27 Accepted Date | 2026-04-28
© Higher Education Press 2026

Coupling Mechanisms of Land Use and Carbon–Heat Risks: A Health–Equity Oriented Study in Hangzhou

Rong XIA[1,2], Yunshan WAN[2,3], Feng QIAN[3], Hao YUAN[3], Yafei ZHAO[2,4], Paolo Vincenzo GENOVESE[2,3,*]

1 School of Landscape Architecture, Zhejiang A&F University, Hangzhou 311300, China
2 International Center of History, Critics of Architecture and Restoration of Historical Heritage (ICHCR), Zhejiang University, Hangzhou 310058, China
3 College of Civil Engineering and Architecture, Zhejiang University, Hangzhou 310058, China
4 School of Smart City Engineering, Qingdao Huanghai University, Qingdao 266427, China

*CORRESPONDING AUTHOR
Address: No. 866, Yuhangtang Road, Xihu District, Hangzhou 310058, China
Email: pavic@zju.edu.cn

GRAPHICAL ABSTRACT

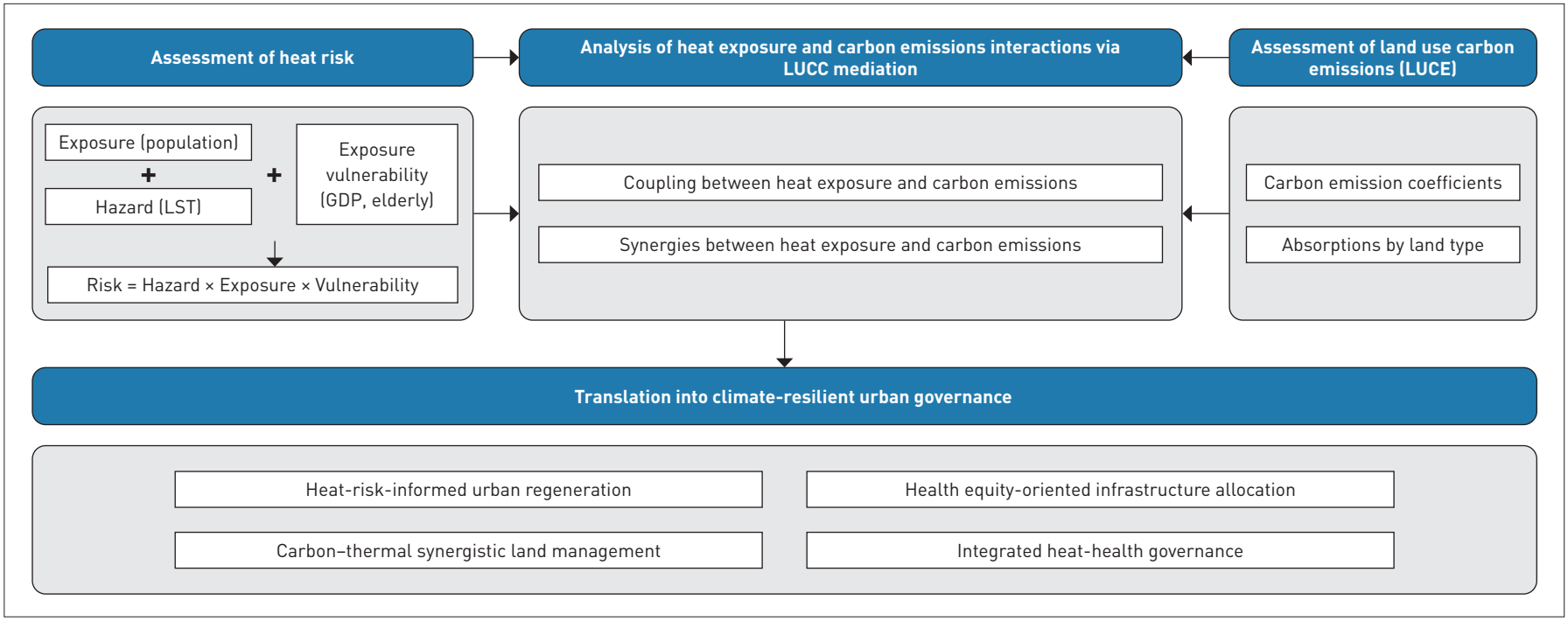

ABSTRACT

Urban land-use transformation simultaneously reshapes carbon dynamics and thermal environments, yet the coupled impacts on urban heat-related health risks remain insufficiently understood. This study develops a Smart Ensemble framework integrating multiple forecasting models to quantify the interactions among land use cover change (LUCC), land use carbon emissions (LUCE), and heat health risks in Hangzhou, China, by combining ensemble land-use prediction, carbon emission accounting, heat health risk assessment, and spatial equity analysis. Future land-use trajectories from 2025 to 2030 were simulated using the framework, while LUCE and the Heat Health Risk (HHR) were quantified to evaluate environmental and social vulnerabilities.

The results reveal substantial spatial heterogeneity in the coupled heat–carbon system. Construction land expansion was identified as the dominant driver of future LUCE growth, with an increase by 2030 due to the conversion of forests and arable lands.

Concurrently, heat health risks exhibited a distinct pattern between old town and new districts. Although urban cores benefit from greater medical accessibility, high population pressure generates potential service mismatches, whereas peripheral districts such as Linping face elevated risks associated with insufficient healthcare and cooling resources. Morphological analysis further demonstrates a nonlinear relationship between street density and heat risk, highlighting the importance of climate-sensitive urban design.

Overall, this study demonstrates that LUCC serves as a critical mediator linking carbon emissions and heat-related health risks. The findings suggest that future urban resilience strategies should move beyond conventional infrastructure expansion toward spatially targeted interventions, including preservation of ecological cooling corridors, optimization of high-density urban morphology, and equitable allocation of heat adaptation resources. This integrated framework provides a quantitative basis for climate-resilient and health-oriented urban planning in rapidly urbanizing regions.

KEYWORDS

Healthy Cities; Urban Heat Exposure; Land Use Cover Change; Carbon Emissions; Climate-Health Nexus

HIGHLIGHTS

- Developed an integrated framework linking land use cover change, carbon emissions, and heat health risks
- Predicted future land-use trajectories using a Smart Ensemble model to improve LUCC simulation robustness
- Revealed that construction land expansion drives carbon emission increases while reducing ecological cooling capacity
- Identified spatial disparities in heat health risks between aging urban cores and emerging peripheral districts
- Demonstrated the role of urban morphology and ecological buffers in mitigating future heat-related risks

RESEARCH FUNDS

- The Scientific Research Start-up Fund of Qiushi Distinguished Professor of Zhejiang University (No. 113000+1944224R1/005)
- Open Research Project of Anhui Provincial Key Laboratory of Huizhou Architecture (No. 513101-W02401)

1 Introduction

1.1 Coupling Mechanisms of Land Use, Carbon Emissions, and Heat Exposure in Healthy City Construction

Global urbanization has precipitated profound environmental transformations, manifesting most critically in the dual challenges of escalating carbon emissions and the intensification of Urban Heat Islands (UHIs)[1]. While traditional urban studies often treat carbon reduction and thermal environment regulation as separate silos, recent theoretical frameworks suggest that they are inextricably linked through a common driver—Land Use and Land Use Cover Change (LUCC)[2]. As the spatial carrier of human activities, LUCC acts as the critical mediating variable in the urbanization–environment–health nexus[3].

The mediating role of land use operates through two distinct but coupled pathways. First, in terms of carbon dynamics, the conversion of natural sinks (e.g., forests, wetlands) into impervious built-up areas fundamentally alters the carbon cycle, shifting the landscape from sequestration to emission sources due to the energy consumption and transportation demands dependent on these land use types[4]. Second, in terms of thermal environments, this same land surface transformation modifies surface energy budgets—specifically through reduced evapotranspiration and increased heat storage in building materials—thereby exacerbating heat risks[5–6]. Consequently, LUCC serves as the physical interface where the goals of "low carbon" and "heat reduction" either conflict or synergize.

Public health constitutes the ultimate endpoint of this environmental cascade. The coupling of high carbon emissions and extreme heat creates a compound health risk, particularly for vulnerable populations[7]. Direct heat exposure leads to increased morbidity from cardiovascular and respiratory diseases (heat-related illness), while carbon-intensive urban forms often correlate with poor air quality and reduced physical activity, further amplifying chronic disease burdens[8]. Therefore, the concept of the "Healthy City" cannot be achieved solely through medical resources but requires a proactive, preventive approach that targets the environmental determinants of health—specifically by optimizing land use to mitigate thermal stress and decarbonize the urban fabric[9].

However, current urban regeneration strategies often lack a systemic understanding of these coupled mechanisms[10–13]. While landscape architecture and urban planning offer tools for intervention—such as green-blue infrastructure (GBI)—there is a paucity of research that quantitatively links land use decisions to their simultaneous health and low-carbon outcomes[14–15]. Moreover,

as cities face uncertain futures, static analyses are insufficient. There is an urgent need to integrate predictive modeling to forecast how current planning decisions will impact the future distribution of heat exposure and carbon footprints. This study addresses these gaps by quantifying the interactions among LUCC, carbon emissions, and heat-related health risks, providing evidence-based insights for climate-resilient and health-oriented urban planning.

1.2 Research on Urban Land Use Models

Traditional urban land use models, such as Cellular Automata (CA) and Markov chains, have been widely employed to capture the spatiotemporal dynamics of land transitions[16–17]. CA models emphasize neighborhood interactions and cellular rules to simulate emergent patterns, while Markov models rely on probabilistic transition matrices derived from historical data to forecast land use demands[18]. Hybrid approaches, like CA-Markov, combine these strengths to enhance accuracy and spatial coherence[14]. More advanced frameworks, such as the Patch-generating Land Use Simulation (PLUS) model[19], incorporate patch-based processes and multi-objective optimization to better replicate complex landscape patterns[20]. Despite these advancements, existing models often face limitations, including sensitivity to initial conditions, computational inefficiencies for large-scale datasets, and inadequate integration of socio-economic drivers like population density and GDP[21–22]. Furthermore, in rapidly urbanized regions such as those in the Global South, models frequently overlook localized vulnerabilities, such as heat exposure risks for elderly populations and land use-induced carbon emissions[23].

1.3 Urban Heat Exposure and Carbon Emission Prediction

Predicting heat exposure driven by urban land use is essential for mitigating UHI effects and enhancing public health resilience amid climate change[24]. LUCC, such as impervious surface expansion and vegetation loss, exacerbate surface and air temperature anomalies, increasing risks of heat-related illnesses in densely populated areas[25]. Machine learning integrated with GIS and remote sensing has emerged as a powerful approach to modeling heat exposure at fine spatial scales, capturing nonlinear relationships between land cover types and thermal dynamics[26]. For instance, hybrid models combining random forests and convolutional neural networks have accurately forecasted land surface temperature (LST) variations in response to land use scenarios, revealing potential reductions in UHI intensity through green infrastructure[27]. Applications in diverse urban contexts, including European and Asian megacities, underscore the efficacy of these methods in simulating diurnal heat patterns and identifying vulnerable hotspots[28]. Furthermore, interpretable frameworks like SHAP-enhanced boosting algorithms have quantified the contributions of land use factors to heat stress[29]. However, persistent challenges include integrating dynamic socio-economic data and multi-scale uncertainties, calling for advanced models that couple thermal feedbacks with real-time observations to refine heat exposure projections[30–31].

Similarly, predicting carbon emissions from urban land use is vital for proactive policy-making and scenario planning[32]. Advanced predictive models, including machine learning algorithms and GIS-based forecasting, enable the estimation of future emissions under various land use scenarios[33]. By quantifying the carbon implications of activities like deforestation, urban expansion, or redevelopment[34], these tools inform strategies to achieve net-zero targets. For example, studies have demonstrated that shifts in land use patterns could significantly reduce urban CO_2 outputs by mid-century[35]. Multi-scale carbon emission characterization and prediction models based on land use, using interpretable machine learning, have been applied in regions like the Yangtze River Delta to forecast emissions accurately[36]. Research also emphasizes the critical role of land-use emissions in meeting climate targets, such as those under the Paris Agreement[37]. Additionally, identifying carbon emission sources in urban land use supports territorial spatial planning, as seen in case studies of cities like Nanjing[38].

This study addresses these interconnected themes by examining the synergies between low-carbon urban construction, land use modeling, and emission forecasting. Through a comprehensive analysis, we aim to provide insights that guide policymakers toward sustainable urban futures, ultimately contributing to global efforts in combating climate change and promoting healthier cities.

2 Research Methods

The technical route of this study comprises five key stages: data acquisition, land use prediction, assessment of heat risk, assessment of land use carbon emissions (LUCE), and analysis of heat exposure and carbon emissions interactions via LUCC mediation (Fig. 1). The Hangzhou metropolitan area was selected as the study region. Multi-source data were collected, including land use datasets, land surface temperature, population density, and socioeconomic indicators. Subsequently, LUCC was simulated using Markov, CA (Cellular Automata), CA-Markov, and PLUS models, and prediction accuracy for 2022–2025 was evaluated with multiple indicators—overall accuracy (OA), Kappa

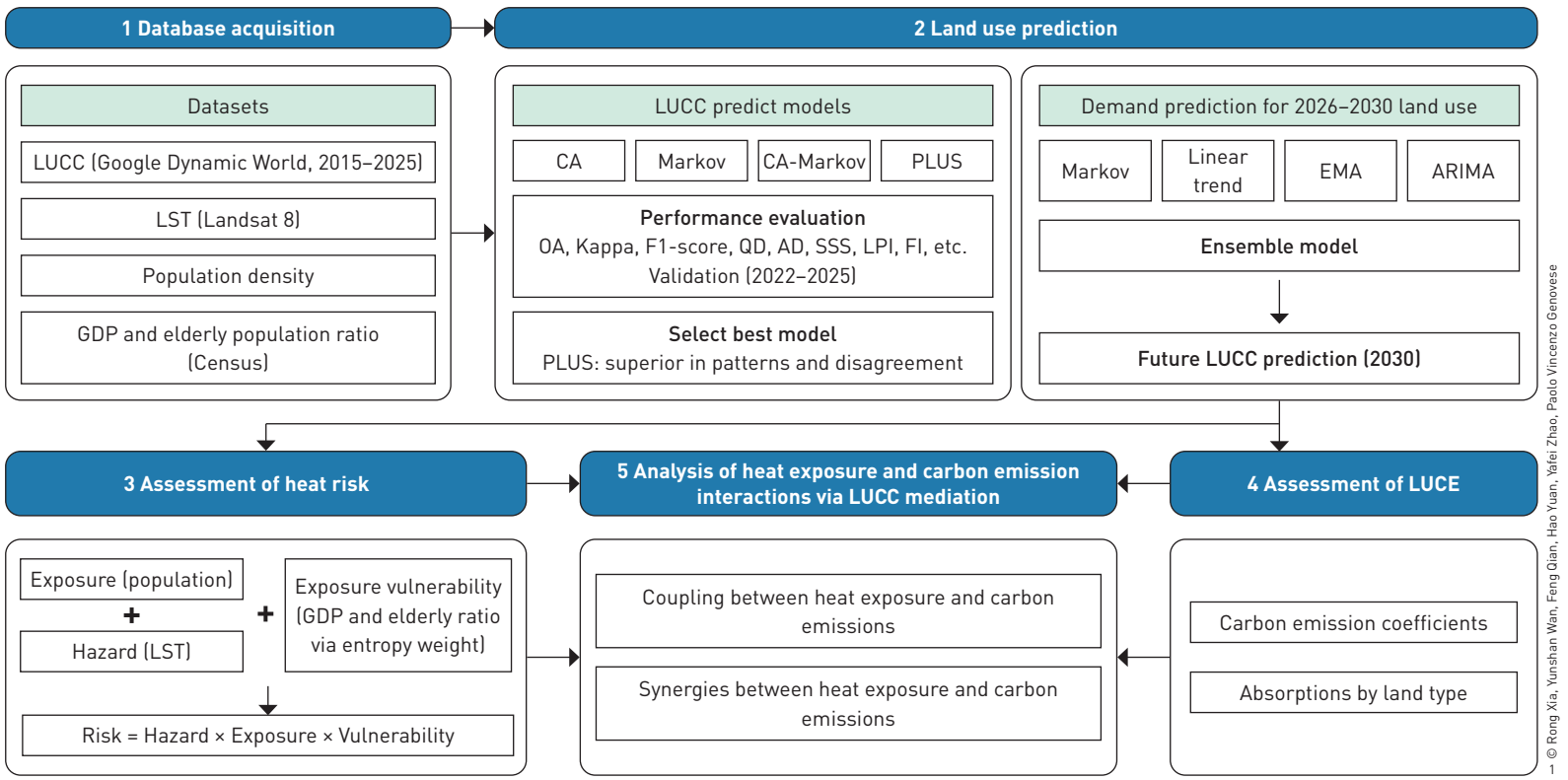

Fig. 1 Technical route of the study.

coefficient (k), F1-score, quantity disagreement (QD), allocation disagreement (AD), spatial structure similarity (SSS), landscape pattern index (LPI), fragmentation index (FI), etc.—confirming the superior performance of the PLUS model in capturing spatial patterns and reducing disagreement. Based on this, future land use demand for 2026–2030 was projected by integrating Markov, linear trend, exponential moving average (EMA), and ARIMA methods, and LUCC scenarios were generated with the PLUS model. On this basis, LUCE and absorption were calculated, while the Heat Risk Index (HRI) was estimated using the Hazard–Exposure–Vulnerability (HEV) framework, a widely applied conceptual framework for climate risk assessment that defines risk as the interaction among climatic hazards, exposed populations or assets, and their vulnerability characteristics[23,39]. Finally, interaction analysis was conducted to reveal the coupling relationships and synergistic effects between LUCE and heat exposure, with LUCC identified as a mediating factor, thereby providing scientific support for subsequent results, policy implications, and the construction of Healthy Cities (Fig. 1).

2.1 Study Area and Data Description

The study focuses on the main urban area of Hangzhou, Zhejiang Province, China, covering eight administrative districts, including Shangcheng, Xihu, Gongshu, Binjiang, Linping, Qiantang, Yuhang, and Xiaoshan, with a total area of approximately 3,383.33 km^{2}① (Fig. 2).

Historical land use cover data for the study area were acquired from the Google Dynamic World dataset, a global near-real-time land cover product generated using Sentinel-2 imagery and a deep learning model. The data were retrieved and processed for multiple time points from 2015, with annual composites created by applying a mode reduction to the “label” band over each calendar

① The total area was the sum of each administration district within the study area, sourced from official release materials accordingly.



Fig. 2 Location map of the selected urban districts in Hangzhou.

year, clipped to the study area's bounding rectangle, and exported at a 10 m spatial resolution. Each dataset was formatted as a 2D NumPy array, with integer values denoting discrete land use classes (0 = water; 1 = trees; 2 = grass; 3 = flooded vegetation; 4 = crops; 5 = shrub/scrub, 6 = built; 7 = bare; 8 = snow/ice), as defined by the Dynamic World classification scheme. These data were subsequently reclassified into six types: arable, forest, grass, water, construction, and unused. Additionally, each annual data package incorporated critical geospatial metadata, including the Affine transformation matrix for georeferencing, the Coordinate Reference System (CRS), and the raster dimensions (width and height). These raster datasets formed the basis for model calibration and future scenario projections.

For the risk assessment components, the following datasets were utilized.

1) Hazard: Hazard represents the intensity of thermal stress on human health, primarily driven by elevated urban microclimates. In this study, LST data were derived from Landsat 8 imagery and reclassified based on LUCC data, serving as the hazard indicator, as it captures surface heat anomalies influenced by land use patterns such as impervious surfaces and vegetation cover.

2) Exposure: Exposure quantifies the number of individuals potentially affected by high temperatures, reflecting population distribution within urban areas. Population density (POP) data, sourced from the Seventh National Population Census of China, were used as the exposure metric, with higher densities indicating greater exposure levels.

3) Vulnerability: Vulnerability assesses the susceptibility of populations to heat stress, incorporating socio-economic and demographic factors. Projected GDP per capita and the ratio of elderly population (> 60 years old) were used as indicators, both derived from the Seventh National Population Census of China.

2.2 Methods

2.2.1 Land Use Prediction Model

LUCC simulation and prediction were performed using a multi-model approach, including a standalone CA model, Markov Chain Model (MCM), coupled CA-Markov model, and PLUS model. Model performance and spatial accuracy were evaluated comprehensively.

The MCM quantified probabilistic transitions between land use types based on the first-order Markov property. The transition probability matrix (TPM), $P = P_{ij}$, defined the probability of type i at time t transitioning to type j at $t + k$ (where k is the prediction interval, typically 2 yr). TPM was derived from historical land use maps (L_e for early year and L_l for later year) as:

$$P_{ij} = \frac{\text{Area}\ (L_e = i \rightarrow L_l = j)}{\text{Area}\ (L_e = i)}. \quad (1)$$

For each pixel, a random number was compared to cumulative probabilities for stochastic assignment, focusing on quantitative predictions of land use areas.

The CA model simulated spatially explicit dynamics on a grid, with states evolving via local interactions. Transition rules were learned from historical patterns using a machine learning classifier (e.g., Random Forest, Gradient Boosting), trained on features including current land use, neighborhood composition (via kernel convolution in a 3 × 3 window), and normalized spatial coordinates (row_ratios, col_ratios) to capture local and broader influences.

The CA-Markov model coupled MCM's quantitative forecasts with CA's spatial allocation. For each pixel in simulations, a random number determined the governing model probabilistically (e.g., 70% CA, 30% MCM), balancing statistical robustness and spatial fidelity.

The PLUS model extended this framework by incorporating patch-based simulations for improved representation of landscape patterns, using similar probabilistic coupling but emphasizing multi-scale drivers and ecological constraints[14].

2.2.2 Performance Evaluation

Simulated land use maps for the target year were compared with observed maps using quantitative metrics from the confusion matrix (computed on flattened, masked arrays via the calculate advanced metrics function) and visual assessments. Key metrics are included in Table 1.

2.2.3 LUCE Estimation

The carbon emission coefficient method was employed to quantify carbon emissions associated with various land-use types in the study area. In accordance with IPCC guidelines and pertinent literature, forestland, grassland, water bodies, and unused land were classified as carbon sinks, whereas construction land and arable land were designated as carbon sources[40]. Drawing from the findings of existing study[41] and IPCC, the carbon emission coefficients for arable land, forestland, grassland, water bodies, and unused land were determined as 0.461, −5.052, −0.949, −0.253, and −0.005, respectively. Indirect LUCE primarily stem from energy consumption and waste management on construction land, encompassing human activities in sectors such as industry, transportation, retail, and accommodation. As reported by Kaili Ru[42], the carbon emission coefficient for construction land is 90.14, derived from equivalent standard coal calculations. Utilizing these

Table 1: Key metrics from the confusion matrix

Metric	Definition/formula	Description
OA	$OA = \frac{\sum_{k=1}^{J} CM_{kk}}{\sum_{i=1}^{J}\sum_{j=1}^{J} CM_{ij}}$	Proportion of correctly classified pixels, where CM_{kk} denotes the diagonal elements of the confusion matrix representing correctly classified pixels, CM_{ij} represents the number of pixels classified from reference type i to predicted type j, and J indicates the total number of types
Kappa k	$k = \frac{P_o - P_e}{1 - P_e}$	Measures agreement beyond chance, where P_o is the observed agreement and P_e is the expected agreement by chance
Precision	$Precision_k = \frac{TP_k}{TP_k + FP_k}$	Proportion of correctly predicted pixels for type k, where TP_k denotes the number of pixels correctly classified as type k, FP_k represents the number of pixels incorrectly assigned to type k from other reference types, and k indicates the land use type
Recall	$Recall_k = \frac{TP_k}{TP_k + FN_k}$	Proportion of reference pixels of type k, where TP_k denotes the number of pixels correctly classified as type k, and FN_k represents the number of pixels belonging to reference type k but incorrectly classified as other types
F1-score	$F1_k = 2 \times \frac{Precision_k \times Recall_k}{Precision_k + Recall_k}$	Harmonic mean of precision and recall for each type; macro-averaged for overall performance
QD	$QD = \frac{1}{N}\sum_{k=1}^{J} \lvert P_{k,actual} - P_{k,predicted} \rvert$	Measures the proportion of misclassified pixels due to quantity mismatch
AD	—	Represents spatial mismatch after adjusting for quantity disagreement, reflecting misallocation of types
SSS	—	Equivalent to OA but emphasizes preservation of spatial arrangement
LPI	$LPI = 1 - \frac{1}{2}\sum_{k=1}^{J} \lvert P_{k,actual} - P_{k,predicted} \rvert$	Quantifies similarity in landscape composition between classification and reference
FI	$FI = \sum_{k=1}^{J} \lvert P_{k,actual} - P_{k,predicted} \rvert$	Evaluates type distribution evenness; lower values indicate better structural preservation

parameters, LUCE within the study area was computed via Eq. (2):

$$C = \sum C_i = \sum S_i \times V_i, \quad (2)$$

where C is total net LUCE; C_i is carbon emission/absorption of different land-use types; S_i is an area of each land use type; and V_i is carbon emission coefficient of different land use types.

2.2.4 Urban Heat Exposure Calculation

Spatial variability in urban heat exposure due to LUCC was quantified using an adapted version of the Crichton Risk Assessment framework, which integrates three core components: hazard, exposure, and vulnerability, calculated as Eq. (3). This framework provides a structured approach to assessing heat-related risks by multiplying these factors, enabling spatially explicit mapping and prediction of heat exposure hotspots under different land use scenarios:

$$\text{Heat risk} = \text{Hazard} \times \text{Vulnerability} \times \text{Exposure}. \quad (3)$$

Specifically, to enhance accuracy and objectivity, vulnerability was computed using an entropy weight method that combined GDP per capita—as a proxy for access to resources and adaptive capacity—and the proportion of elderly residents, who exhibit reduced physiological resilience to heat. The entropy weight method assigns objective weights based on information entropy, reducing subjectivity compared to equal weighting approaches:

$$Entropy(E_j) = -\left(\frac{1}{\ln n}\right)\sum i = 1^{n} p_{ij} \ln p_{ij}, \quad (4)$$

$$Weight(W_j) = (1 - E_j) / \sum_{k=1}^{m} (1 - E_k), \quad (5)$$

$$Vulnerability = \sum j = 1^{m} W_j \times X_{nor,j}, \quad (6)$$

where p_{ij} is the proportion of the i-th unit's j-th indicator value, n is the number of units, m is the number of indicators (GDP and elderly proportion), and $X_{nor,j}$ is the normalized value of the j-th indicator.

To ensure comparability and avoid zero values that could distort multiplicative results, all indicators (LST, POP, GDP, and elderly proportion) were normalized using a min-max scaling adjusted to a range of 0.1–0.9, preventing underestimation in low-variability scenarios:

$$X_{nor} = 0.1 + \left[(X_{ij} - X_{\min}) / (X_{\max} - X_{\min}) \right] \times 0.8, \quad (7)$$

where X_{nor} is the normalized value, X_{ij} is the original value for the i-th unit and j-th indicator, and $X_{\min}/X_{\max}$ is the minimum/maximum values across the dataset.

For predictive enhancement, the framework was integrated with machine learning to forecast future heat risk under land use scenarios. An XGBoost model, trained on historical LST, LUCC data, and socio-economic variables, predicted LST variations, incorporating nonlinear interactions via SHAP interpretability to quantify feature contributions (e.g., impervious surface ratio, NDVI). This optimization improves upon static assessments by enabling scenario-based projections, such as urban expansion or green infrastructure implementation.

The HRI was then calculated to aggregate and categorize risks into five levels (1 = lowest; 5 = highest) for spatial visualization and comparison across scenarios:

$$\text{HRI} = \sum_{i=1} (P_i \times A_i) / S, \quad (8)$$

where P_i is the assigned risk level i, A_i is the area with that level, and S is the total study area. This index facilitates policy-oriented outputs, such as identifying priority zones for intervention. All computations were performed in a GIS environment (e.g., ArcGIS, QGIS) coupled with Python libraries (e.g., scikit-learn for entropy weighting, XGBoost for prediction), ensuring reproducibility and scalability.

3 Research Results and Discussion

3.1 Comparison of Different LUCC Prediction Models

The simulation process was conducted for four land use prediction approaches, including CA, Markov, CA–Markov, and PLUS models. The simulation was initialized using the land use raster of the base year and iteratively updated according to the corresponding transition rules and spatial allocation mechanisms of each model. For model validation, the number of simulation iterations was set according to the temporal interval between the base year and validation year (i.e., two iterations in this study).

To significantly enhance computational efficiency, especially when dealing with large raster datasets, the entire simulation grid was divided into smaller, manageable blocks (e.g., block_size of 512 × 512 pixels). The processing of these individual blocks was then parallelized across multiple CPU cores using the joblib library. Each block's calculation incorporated a padding (or halo) around its boundaries to ensure that neighborhood computations for cells near block edges were accurate and considered data from adjacent blocks.

Upon completion of the final simulation iteration, a crucial post-processing step was applied: a sieve filter. This spatial filtering technique removes small, isolated patches of pixels (e.g., size = 4, meaning patches smaller than 4 pixels) from the predicted land use maps. This step effectively smooths the output, reducing noise and artifacts that can arise during the iterative simulation process, thereby enhancing the spatial coherence and realism of the simulated landscapes.

The validation of the four models was conducted using observed land use data from 2022 to 2025. The results of key performance metrics of the predicted and actual land cover maps are summarized in Fig. 3.

The CA model achieved an *OA* of 0.9002, with a *k* of 0.8402, indicating substantial agreement beyond chance. The *F1-score* was 0.6485, reflecting moderate precision (0.7458) and recall (0.6140) in detecting land use changes. *SSS* was 0.9002, while the *LPI* reached 0.9320, suggesting good preservation of overall landscape configurations. Disagreements were low, with *QD* at 0.0181 and *AD* at 0.0317. The *FI* was 0.0362, indicating relatively low patch fragmentation in predictions.

For the Markov model, the *OA* was 0.8909, accompanied by a *k* of 0.8187. The *F1-score* was lower at 0.5416, driven by precision of 0.6905 and recall of 0.5315. *SSS* stood at 0.8909, and the *LPI* was 0.9223. *QD* was 0.0277, *AD* was 0.0314, and the *FI* was 0.0554, showing slightly higher fragmentation compared to other models.

The CA-Markov hybrid model exhibited an *OA* of 0.8995 and a *k* of 0.8385. The *F1-score* was 0.5883, with precision at 0.7721 and recall at 0.5717. *SSS* was 0.8995, and the *LPI* was 0.9309. *QD* and *AD* were 0.0191 and 0.0314, respectively, while the *FI* was 0.0382.

In contrast, the PLUS model demonstrated an *OA* of 0.9222 and a *k* of 0.8326. The *F1-score* was 0.6430, with balanced precision

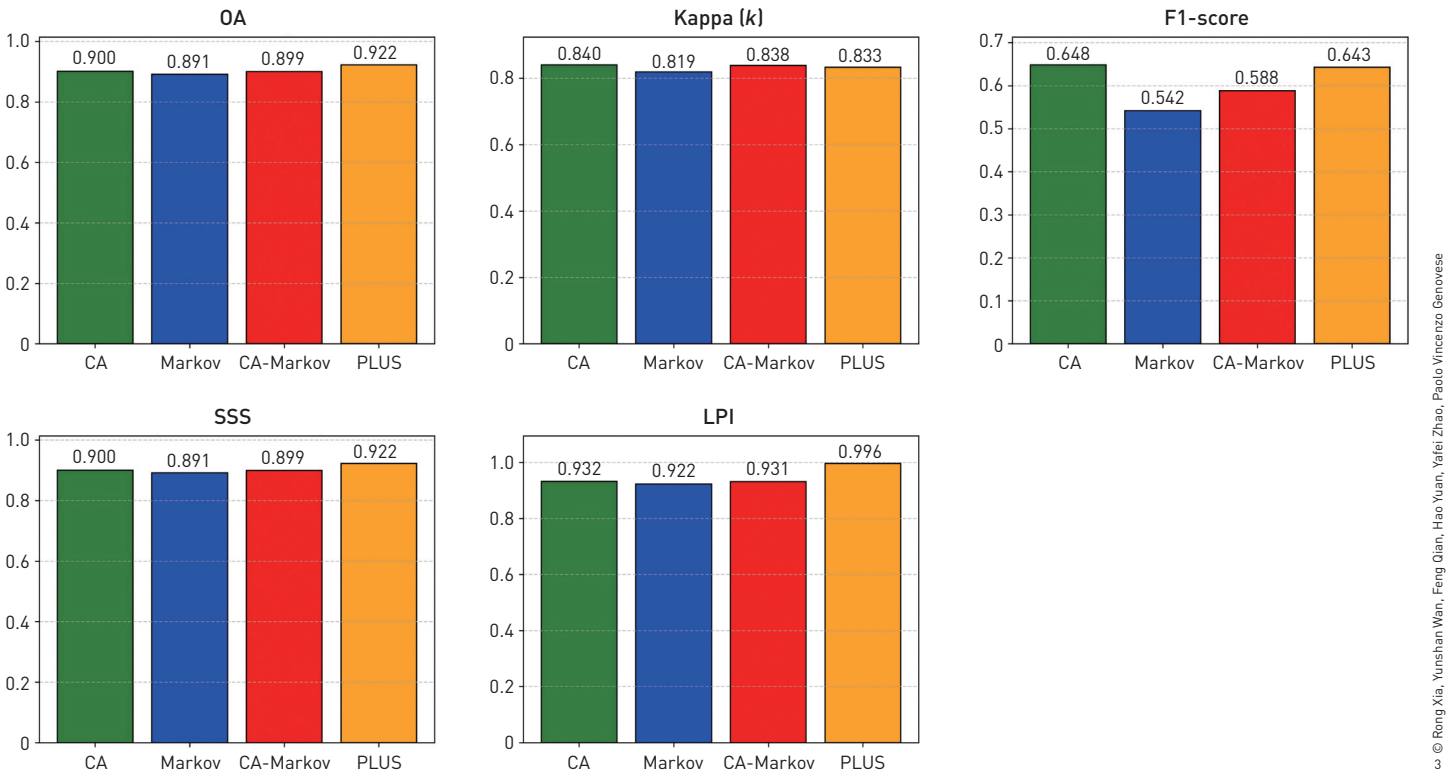

© Rong Xia, Yunshan Wan, Feng Qian, Hao Yuan, Yafei Zhao, Paolo Vincenzo Genovese

Fig. 3 Performance comparison among different LUCC prediction models.

(0.6424) and recall (0.6442). Notably, *SSS* was 0.9222, and the *LPI* was the highest at 0.9955, indicating superior replication of landscape patterns. *QD* was minimal at 0.0045, though *AD* was higher at 0.0733. The *FI* was the lowest at 0.0090, suggesting excellent performance in maintaining patch integrity.

Overall, the models exhibited high accuracy levels (> 0.89), with PLUS demonstrating superior performance in replicating landscape patterns and minimizing quantity disagreement, whereas the CA-based models showed comparable results in terms of spatial agreement and Kappa metrics. Finally, this study utilized land use data from 2015–2024 to predict 2025 land use patterns with each model, followed by error identification against actual 2025 land use data (Fig. 4)[②]. The results further validated the effectiveness of PLUS in this scenario.

3.2 Land Use Prediction

3.2.1 Comparative Evaluation of Forecasting Models

To overcome the limitations of traditional Markov Chain methods—which rely solely on two time points and often yield unstable projections—this study employed a multi-model approach using pixel-level historical data from 2016 to 2025. Four distinct forecasting algorithms (Markov Chain, Linear Trend, EMA, and enhanced ARIMA) were rigorously evaluated using annual land use statistics.

Model performance was assessed via Mean Absolute Error (MAE) and Mean Absolute Percentage Error (MAPE) (Fig. 5) across different land use types: arable land (T1), forest land (T2), grassland (T3), water body (T4), construction land (T5), and unused land (T6). The validation results revealed significant heterogeneity in model suitability across different land use types. The Linear Trend model proved most effective for land types characterized by steady, directional change (T1 and T3), and T3 achieving the lowest system-wide MAE. Conversely, the EMA demonstrated superior performance for types with fluctuating or seasonal patterns (T2 and T4), minimizing prediction error by effectively weighting recent data points. These findings underscore that no single deterministic model can capture the complex dynamics of all land use categories simultaneously, necessitating an integrated approach.

3.2.2 Construction of the Smart Ensemble Framework

Building on the validation results, a smart ensemble framework

② In the figure, model predictions were initially generated using the original nine-class Dynamic World land use scheme and were subsequently reclassified into the six aggregated land use categories used in this study. This post-classification aggregation reduced confusion among spectrally or functionally similar classes and therefore improved the agreement between simulated and observed land use patterns. In the prediction and error maps, the horizontal and vertical axes represent raster column and row indices, respectively, with the origin located at the upper-left corner of the raster. Thus, the vertical coordinate increases from top to bottom and indicates pixel position rather than geographic coordinates.

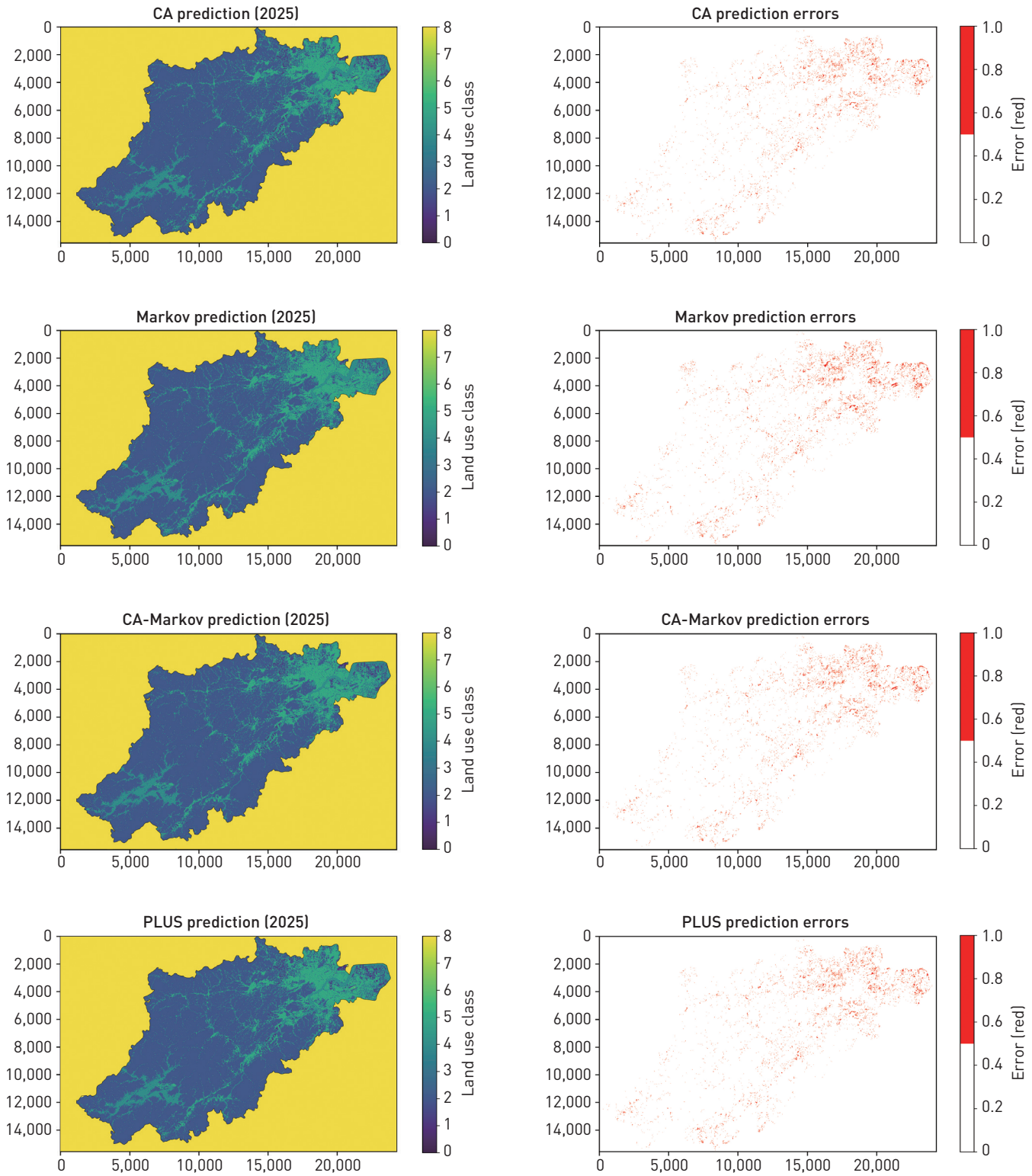

Fig. 4 Various models' comparison of 2025 land use of the selected urban districts of Hangzhou.

was constructed to enhance prediction robustness. Unlike conventional methods that select a "best fit" model, this framework integrates all four models using a dynamic weighting system based on the inverse of their validation MAE. This ensures that models with lower historical errors contribute more significantly to the final projection.

By synthesizing the continuous historical trends (2016–2025) rather than relying on discrete intervals, the ensemble model significantly smoothed the stochastic noise inherent in individual algorithms (Fig. 6). This methodological innovation addresses the instability issues of the standard PLUS model framework, providing a statistically rigorous baseline for future scenario simulation.

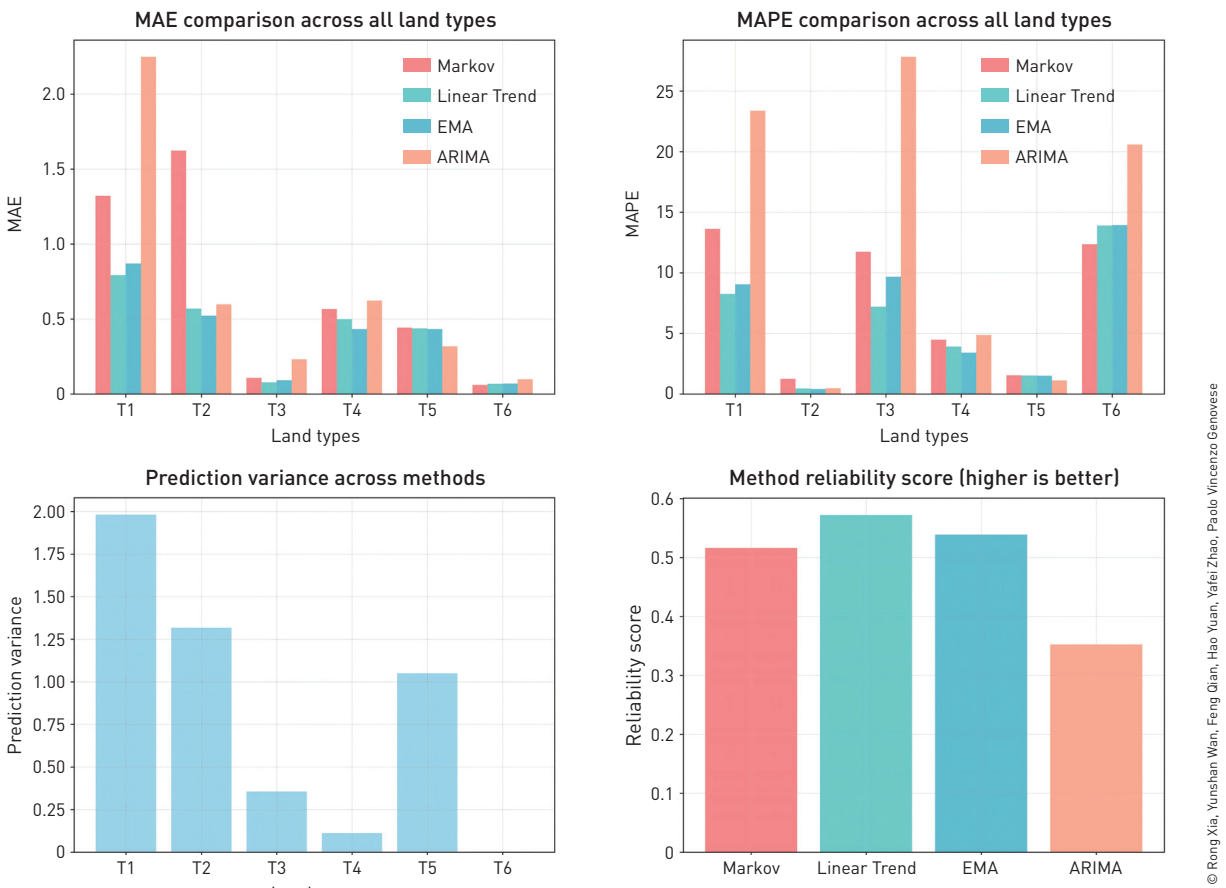

© Rong Xia, Yunshan Wan, Feng Qian, Hao Yuan, Yafei Zhao, Paolo Vincenzo Genovese

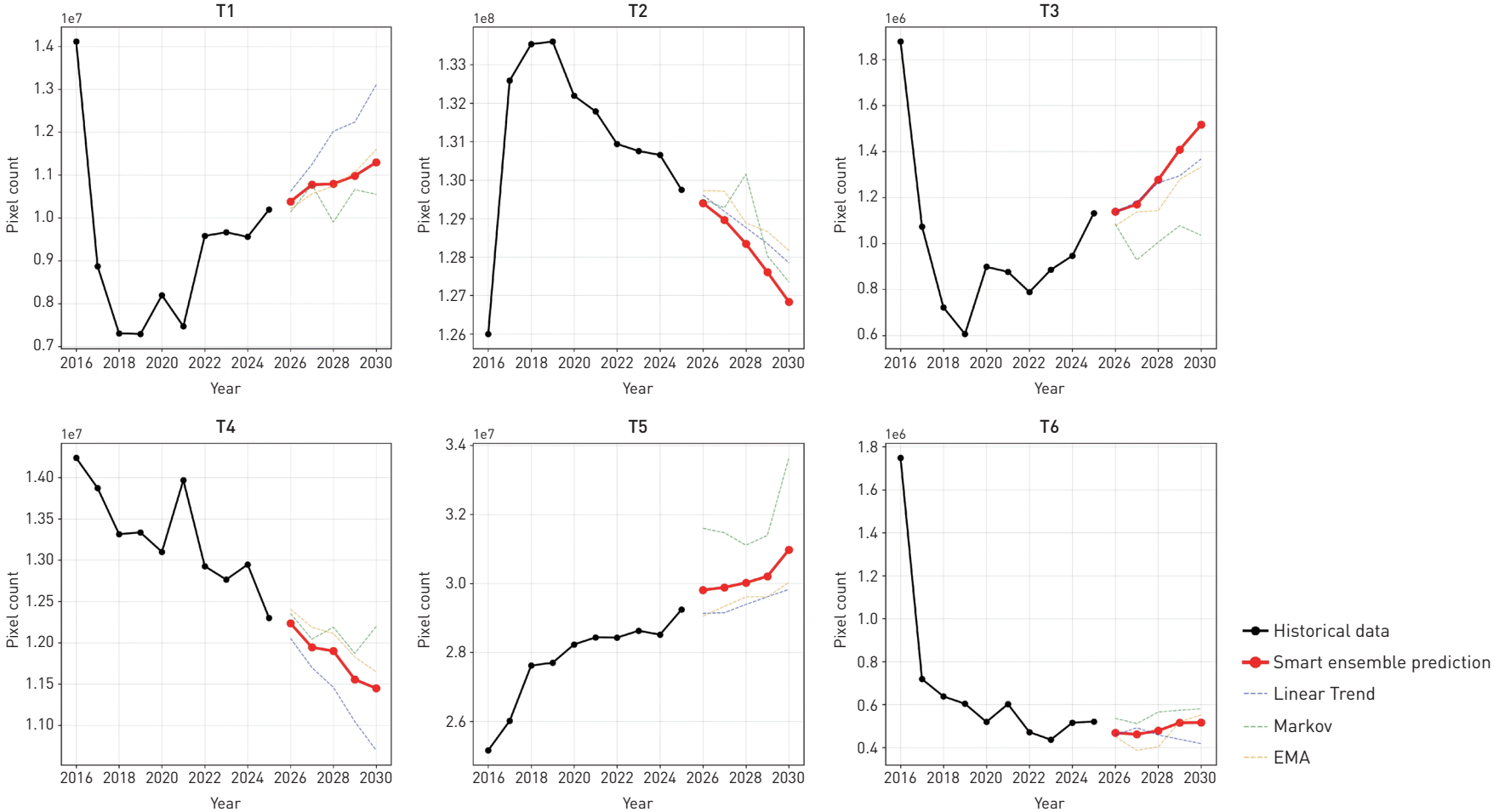

© Rong Xia, Yunshan Wan, Feng Qian, Hao Yuan, Yafei Zhao, Paolo Vincenzo Genovese

Fig. 5 Performance of various demand predict methods for each land type.

Fig. 6 Demand prediction results of ensemble integrated model.

3.2.3 Projected Land Use Trajectories and Development Implications

The ensemble predictions for 2026–2030 indicate heterogeneous trajectories among the six land use types, characterized primarily by the expansion of arable land (T1), grassland (T3), and construction land (T5), accompanied by varying degrees of contraction in forest land (T2), water body (T4), and unused land (T6).

Expansion of arable land, grassland, and construction land: Arable land is projected to increase from 10.47 million pixels in 2026 to 11.20 million pixels in 2030, representing an increase of approximately 6.9%. Grassland exhibits the highest relative growth, increasing by 39.2%, from 1.17 million to 1.63 million pixels. Construction land is also expected to expand steadily, increasing by approximately 3.7%, from 29.55 million to 30.63 million pixels. The continued expansion of construction land reflects ongoing urban development, whereas the increases in arable land and grassland suggest a concurrent redistribution of agricultural and vegetated land.

Contraction of forest land and water bodies: Forest land is projected to decrease slightly from 129.13 million pixels in 2026 to 128.75 million pixels in 2030, corresponding to a decline of approximately 0.3%. In contrast, water bodies show a more pronounced decrease of 7.4%, declining from 12.26 million to 11.35 million pixels. The projected reduction in water area may have important implications for regional ecological regulation, carbon cycling, and urban thermal conditions.

Unused land remains broadly stable at around 0.5 million pixels throughout the prediction period from 2026 to 2030. Despite minor year-to-year fluctuations, no substantial change is observed over the prediction period, indicating an overall stable trend.

Overall, the projected land use pattern is not characterized by a uniform conversion of ecological land into built-up surfaces, but rather by differentiated changes among individual land use types. The simultaneous expansion of construction land and reduction in forest and water areas may nevertheless intensify carbon emissions and heat exposure risks, while changes in arable land and grassland may modify regional carbon sequestration and surface energy exchange. These projections therefore provide essential spatial boundary conditions for the subsequent assessment of LUCE and urban heat exposure.

3.3 Urban Heat Exposure and Carbon Emission Estimation

Trend analysis, based on change rates from the ensemble predictions, indicates divergent trajectories across land use types. These patterns align with the optimized model's emphasis on recent historical fluctuations, enhancing reliability over single-method approaches. The integration of multi-year pixel statistics via direct Python Markov Chain computation addressed software framework limitations, improving overall robustness as evidenced by reduced MAPE in the ensemble compared with individual models.

3.3.1 Urban Heat Exposure Prediction

Following the min-max normalization (0.1–0.9 range) of all input indicators, the composite urban heat exposure was calculated by integrating hazard (LST), exposure (POP), and vulnerability (GDP and elderly population ratio) through a multiplicative framework. This normalization ensured comparability across the 34,562,995 valid pixels and prevented nullification in the final risk product. As established via the entropy weight method, demographic factors—specifically the elderly population ratio (weight = 0.8667)—dominate the vulnerability dimension over economic sensitivity (weight = 0.1333). This weighting mechanism heavily penalizes areas with concentrated aging populations, directly amplifying their composite heat risk.

Spatial reconstruction and district-level statistical aggregation (Fig. 7) reveal stark geographical heterogeneity across the study area. The risk distribution is heavily skewed toward the historic urban cores, driven by the synergistic overlap of all three risk components.

1) Hazard and exposure concentration: Gongshu and Shangcheng districts exhibit the highest thermal hazard intensities, with mean values of 0.770 and 0.758, respectively. These districts simultaneously record the highest exposure means (0.335 and 0.326), reflecting intense population density within the urban center. In contrast, extensive peripheral districts like Yuhang record the lowest baseline hazard (0.698) and exposure (0.127).

2) Vulnerability amplification: Driven by the high elderly population ratio weight, vulnerability scores peak in Gongshu (mean = 0.314) and Shangcheng (mean = 0.281). This demographic clustering acts as a critical risk multiplier. For instance, while Binjiang sustains a relatively high hazard mean (0.740), its lower vulnerability (0.174) significantly dampens its overall risk profile (mean heat risk = 0.034).

3) Composite risk distribution: The multiplicative effect culminates in Gongshu recording the highest mean heat risk (0.100), followed closely by Shangcheng (0.083). The statistical variance within these core districts—such as Gongshu's mean (0.100) significantly exceeding its median (0.061)—indicates a right-skewed distribution. This confirms the presence of acute, localized micro-hotspots rather than uniformly distributed thermal stress across the study area.

Conversely, transitioning and peripheral zones exhibit a pervasive but low-intensity risk profile. Xiaoshan represents the largest spatial

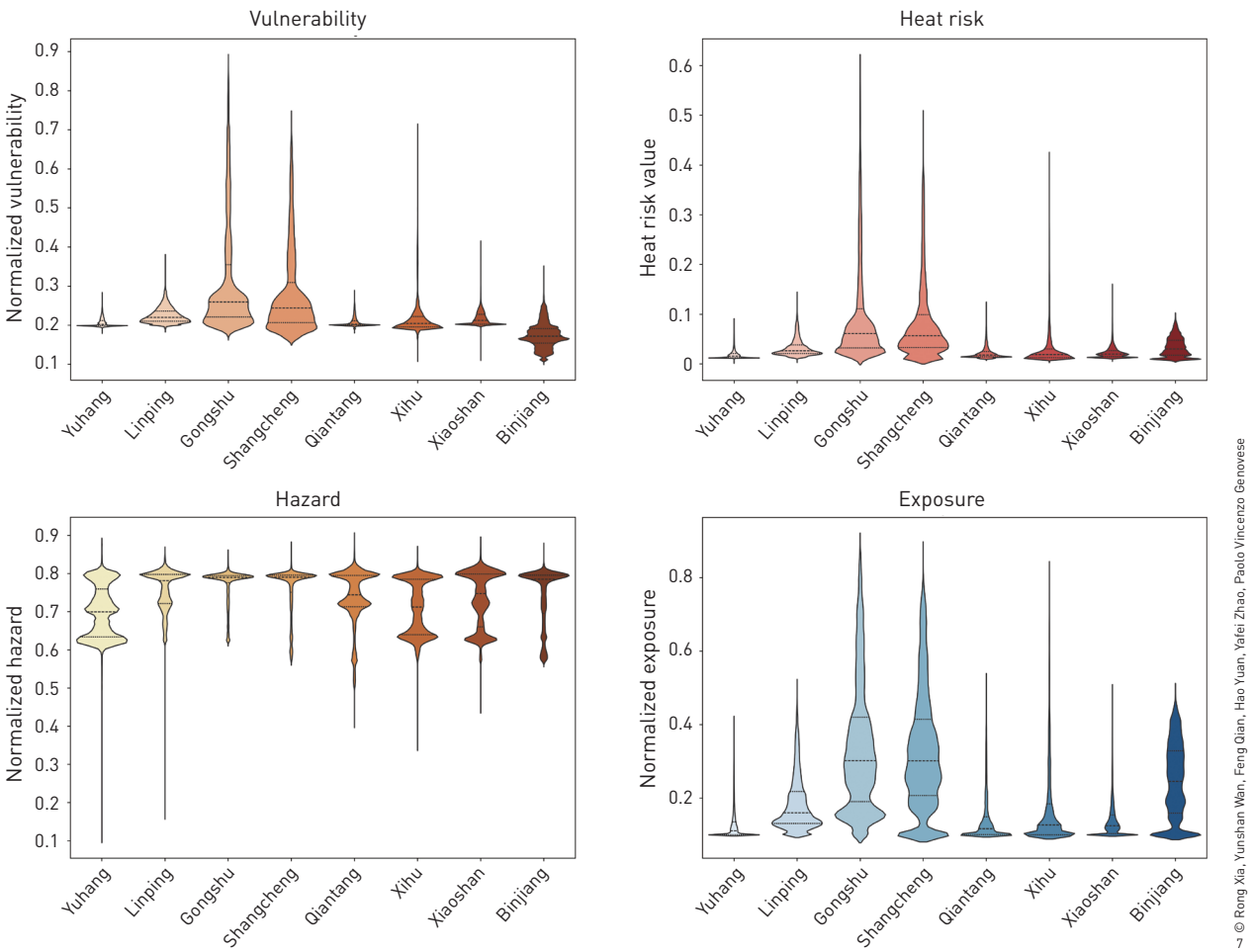

© Rong Xia, Yunshan Wan, Feng Qian, Hao Yuan, Yafei Zhao, Paolo Vincenzo Genovese

Fig. 7 Urban heat exposure prediction of the selected urban districts of Hangzhou.

footprint in the study area but maintains a highly constrained mean heat risk of 0.024. Similar baseline profiles are observed in Qiantang (0.022) and Yuhang (0.019). Linping presents a transitional anomaly: it sustains a high thermal hazard (mean = 0.756, approaching core levels) but records a moderate mean heat risk (0.033) due to currently constrained exposure (0.185) and vulnerability (0.225) metrics.

These findings indicate that while thermal hazards (LST gradients) are broadly distributed across the urban–rural continuum, critical heat risk is highly localized. The component distribution underscores the framework's capacity to capture synergistic environmental–demographic interactions, establishing a quantitative baseline that prioritizes the aging urban core for immediate spatial equity restoration and heat adaptation interventions.

3.3.2 Carbon Emission Calculation

The total administrative area of the study region, delineated according to official administrative boundaries, was approximately 338,333 hm^2. However, after accounting for the spatial coverage of valid Google Dynamic World land-cover data, the effective area available for analysis was 334,845.99 hm^2. Accordingly, all subsequent area-based calculations were performed using 334,845.99 hm^2 as the reference area.

Land use areas in 2025 and 2030 are summarized in Fig. 8. Construction land dominated both periods, accounting for 46.0% (154,024.14 hm^2) in 2025 and increasing to 47.8% (160,029.88 hm^2) in 2030. Forest land was the second largest category, decreasing from 25.5% (85,527.83 hm^2) to 24.9% (83,537.81 hm^2). Arable land also declined from 15.3% (51,204.98 hm^2) to 14.2% (47,442.53 hm^2). Minor reductions were observed in grassland (from 2,612.85 hm^2 to 2,240.92 hm^2), unused land (from 3,055.34 hm^2 to 3,028.85 hm^2), and a slight increase in water bodies (from 38,420.85 hm^2 to 38,566.00 hm^2).

The largest absolute area change was in construction land (+6,005.74 hm^2), followed by decreases in arable land (−3,762.45 hm^2) and forest land (−1,990.02 hm^2). These shifts indicate a trend toward urbanization, with natural and agricultural lands converting to built-up areas.

Total LUCE increased from 13,463,039.53 tC/yr in 2025 to 14,013,032.40 tC/yr in 2030, resulting in a net increase of 549,992.86 tC/yr (Table 3). This net positive change reflects an overall rise in carbon emissions, primarily driven by expansion of

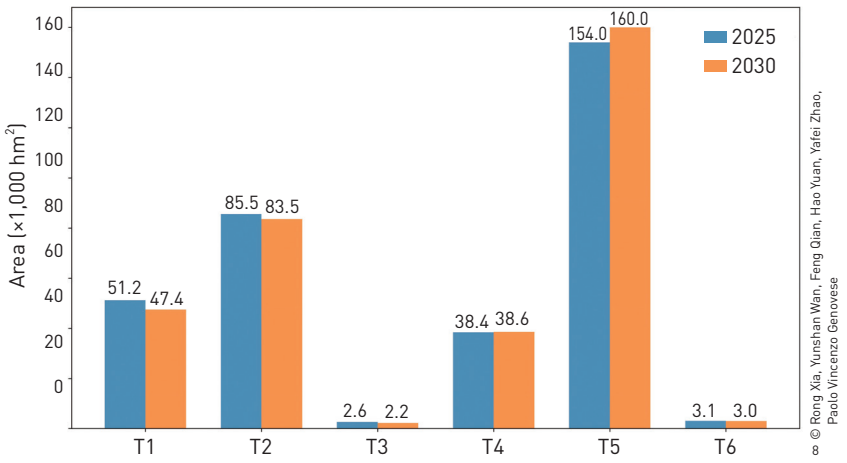

Fig. 8 Bar charts of land use area change between 2025 and 2030.

high-emission construction land.

LUCE values varied markedly by land type due to differing emission coefficients. Construction land was the dominant emission source, contributing 13,883,735.98 tC/yr in 2025 and 14,425,093.38 tC/yr in 2030 (102.9% of net LUCE), with a high emission coefficient of 90.14 tC/hm^2/yr. The proportion exceeding 100% reflects that construction land emissions represent gross carbon emissions, whereas carbon sequestration from forest land, grassland, water bodies, and unused land offsets part of these emissions, thereby reducing the final regional net LUCE. In contrast, forest land acted as the primary carbon sink, absorbing −432,086.60 tC/yr in 2025 and −422,033.02 tC/yr in 2030 (coefficient = −5.052 tC/hm^2/yr). Other sinks included grassland (−2,479.59 to −2,126.63 tC/yr), water bodies (−9,720.48 to −9,757.20 tC/yr), and unused land (−15.28 to −15.14 tC/yr). Arable land was a minor emitter (23,605.50 to 21,871.01 tC/yr; coefficient = 0.461 tC/hm^2/yr).

Because LUCE magnitudes spanned several orders of magnitude and included both positive emissions and negative sequestration values, Fig. 9 presents their magnitudes using an appropriate logarithmic representation while retaining the distinction between carbon sources and sinks. Construction-land emissions were on the order of 10^7 tC/yr, whereas the absolute LUCE values of the remaining land-use categories ranged approximately from 10^1 to 10^5 tC/yr.

Land-use transitions were further examined using a scaled transition matrix derived from 500,000 sampled cells, corresponding to approximately 0.57% of the 87,656,928 raster cells. Four major transitions with estimated converted areas exceeding 1,000 hm^2 were identified: arable land to forest land (1,402 hm^2), arable land to construction land (4,107 hm^2), forest land to arable land (1,464 hm^2), and forest land to construction land (2,979 hm^2). The corresponding LUCE impacts should be calculated using the full-precision emission coefficients used in the model.

Conversions to construction land generated the largest positive carbon impacts, whereas conversion from arable land to forest land produced a negative LUCE effect through enhanced carbon sequestration. Although the four major transitions accounted for most of the large individual LUCE changes, smaller land-use transitions generated additional offsetting effects. When all transition pathways were considered, the resulting net effect was consistent with the approximately 550,000 tC/yr increase in regional LUCE between 2025 and 2030.

Overall, projected LUCC from 2025 to 2030 is characterized by expansion of construction land and contraction of forest and arable land, resulting in an increase of approximately 0.55 million tC/yr in net LUCE. These findings underscore the carbon implications of land conversion patterns.

3.4 Analysis of Interaction Mechanisms Between Urban Heat Exposure and Carbon Emissions

3.4.1 LUCC as a Mediator: The Structural Nexus of Heat and Carbon

Based on the integrated projections of urban heat exposure and LUCE, this section elucidates the coupling mechanisms within the Hangzhou metropolitan area for the 2025–2030 period. The analysis reveals that the correlation between heat risk and carbon emissions is not merely a spatial coincidence but is fundamentally mediated by LUCC. LUCC acts as the primary intermediary that simultaneously dictates the surface energy balance (affecting LST)

Fig. 9 LUCE/absorptions (log scale) between 2025 and 2030.

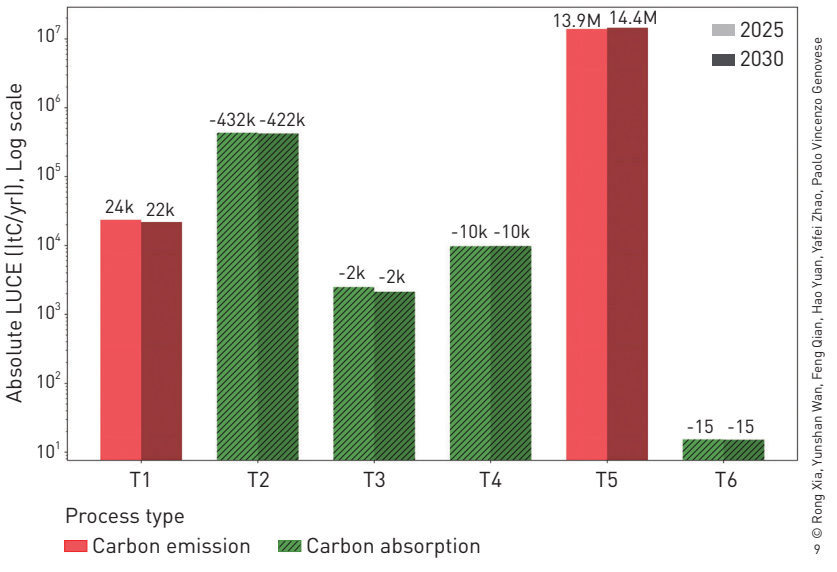

and the carbon flux (affecting LUCE)[4,29].

Specifically, the expansion of construction land—projected to be the dominant land transformation—functions as a dual-driver. On the one hand, it replaces natural carbon sinks with emission-intensive urban surfaces, thereby escalating net LUCE. On the other hand, the replacement of pervious, vegetated surfaces with high-thermal-capacity impervious materials directly elevates LST through the reduction of evaporative cooling and altered albedo[6]. Consequently, the projected shift from forest and arable lands to construction areas creates a synchronized surge in both localized thermal hazard and regional carbon footprints, establishing LUCC as the structural nexus of these two environmental stressors.

3.4.2 Direct and Inverse Coupling via Land Surface Properties

The interaction between heat exposure and carbon emissions manifests through complex coupling pathways dependent on land use characteristics. Direct coupling is observed in high-density urban cores where construction land expansion serves as a hotspot for both carbon sources and thermal accumulation. In these zones, the elderly population ratio and POP—key components of the HRI—overlap with carbon-intensive infrastructure. Every unit of expanded construction land not only boosts energy-related emissions but also amplifies the UHI effect, creating a spatially concentrated risk profile[35,43].

Conversely, inverse coupling is driven by the loss of natural land (forests and water bodies). These land types provide critical "cooling buffers" through transpiration and serve as vital carbon sinks. The results indicate that as forest cover declines, the simultaneous loss of sequestration capacity and thermal regulation leads to an "environmental double-jeopardy": a rise in net carbon emissions paired with an increase in localized HRI. This relationship highlights that the synergy between heat and carbon is contingent upon the ecological integrity of the land use matrix, where the depletion of GBI erodes the city's climate resilience[35].

3.4.3 Synergistic Feedback and Cascade Effects

Furthermore, the interaction between heat and carbon emissions is characterized by a positive feedback loop mediated by socioeconomic drivers. The study identifies a "UHI–carbon synergy" where elevated LST in high-risk zones necessitates increased energy consumption for cooling, which in turn elevates anthropogenic carbon emissions, further exacerbating the regional greenhouse effect and localized warming[44].

This synergy is amplified by spatial heterogeneity: the highest HRI values are projected in areas with the most significant "source–sink" imbalances—where emission sources (construction land) are maximized and cooling buffers (forest land) are marginalized. From a public health perspective, this means that vulnerable population (e.g., the elderly in urban cores) are not only exposed to higher temperatures but are also situated in environments with the highest carbon-intensive development, leading to compounded environmental health burdens. In summary, the future trajectories of HRI and LUCE are intrinsically interdependent, with LUCC serving as the decisive mediator that either exacerbates or mitigates this compound climate risk.

3.5 Spatial Differentiation, Attribution, and Equity Evaluation of Urban Heat Health Risk

3.5.1 Spatial Differentiation of Comprehensive Heat Health Risk and Agglomeration of Social Vulnerability

Based on district-level statistics (Fig. 10), the comprehensive Heat Health Risk (HHR) across the study area exhibits significant spatial heterogeneity. The data indicate that high-risk urban zones are shaped by the dual superposition of thermal exposure and population concentration. These core areas operate not only as physical "heat islands" but also as "vulnerability islands" where susceptible populations are heavily concentrated, exacerbating urban health inequality.

This spatial imbalance manifests as a distinct "old city–new district" duality. Gongshu District, functioning as a typical aging central urban area, records the highest mean HHR (0.590) and serves as the core of the region's heat health pressure. This elevated composite risk is driven by intense LSTs (mean LST = 0.869) coupled with the highest population exposure in the city (mean POP = 0.298). Shangcheng District follows closely with a mean HHR of 0.558, displaying a parallel pattern of high thermal exposure (mean LST = 0.856) and population concentration (mean POP = 0.275).

Beyond the core HHR components, three supplementary indicators were introduced to investigate the spatial mechanisms underlying heat-health inequality: distance to medical facilities, medical resource supply–demand pressure, and street network density. These variables were not used in the calculation of HHR; instead, they were employed to characterize healthcare accessibility, service adequacy, and urban morphological conditions, respectively. Medical-facility distance captures the spatial accessibility of healthcare services, while the supply–demand pressure index identifies areas where available medical resources may be insufficient relative to population demand. Street network density serves as a morphological proxy for urban compactness and development intensity, providing additional insight into the built-environment conditions associated with thermal

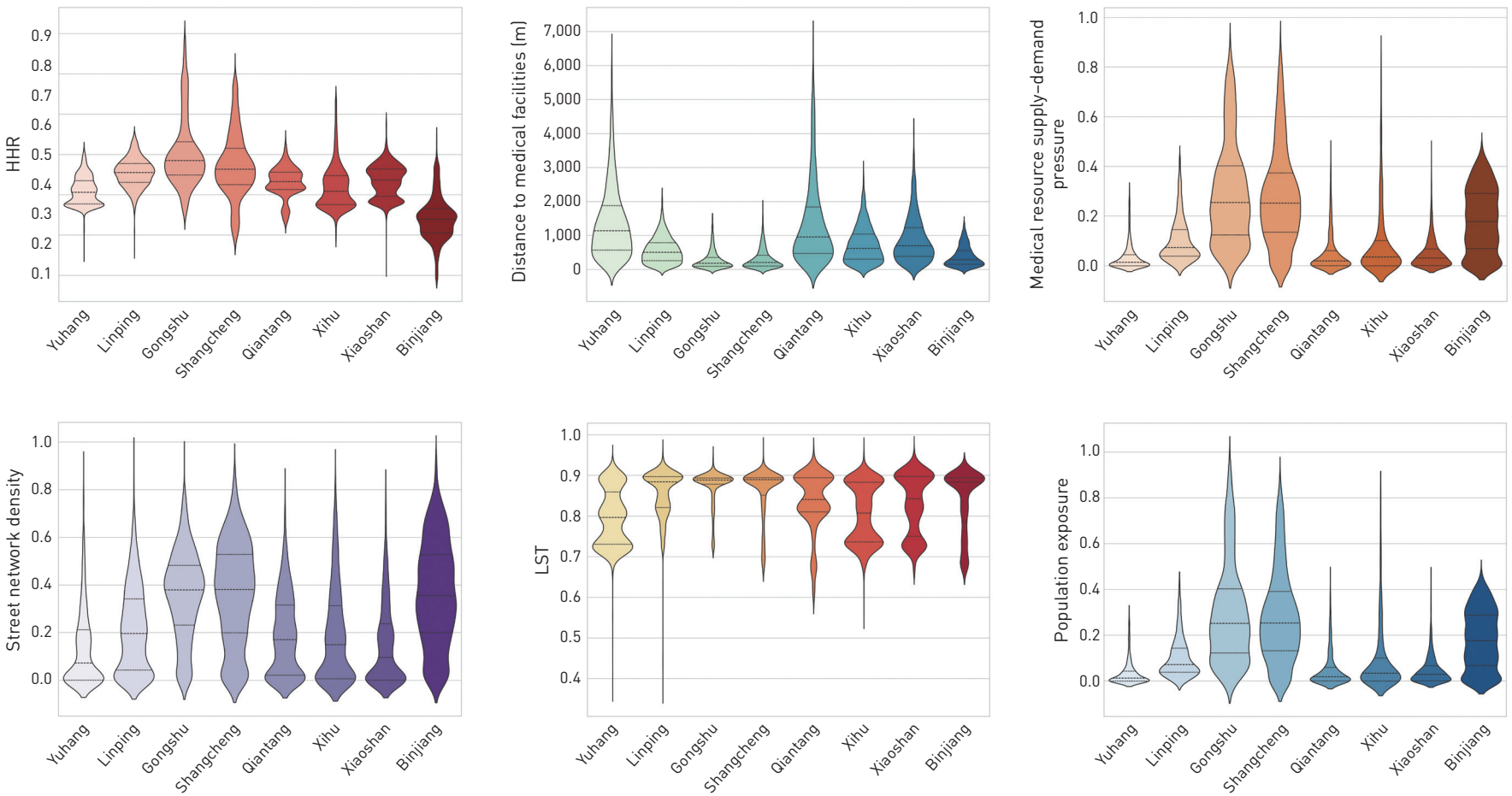

© Rong Xia, Yunshan Wan, Feng Qian, Hao Yuan, Yafei Zhao, Paolo Vincenzo Genovese

Fig. 10 Spatial health equity analysis of the selected urban districts of Hangzhou.

accumulation. Their joint assessment with HHR, LST, and population exposure enables a more comprehensive interpretation of the environmental, infrastructural, and morphological dimensions of urban heat-health risk.

While these central districts possess the shortest physical distances to medical facilities (Gongshu: 288.6 m; Shangcheng: 321.3 m), they simultaneously endure the highest medical supply–demand pressures (0.294 and 0.269, respectively) (Fig. 10). This demonstrates that the extreme agglomeration of social vulnerability and population density heavily offsets the spatial advantages of facility proximity.

In contrast, Binjiang District, representing an emerging development zone, maintains the lowest mean HHR (0.442). Despite recording the highest average street density (0.371) and substantial thermal exposure (mean LST = 0.839), its significantly lower population exposure index (0.183) effectively buffers the overall composite risk. Conversely, peripheral districts such as Yuhang and Qiantang exhibit moderate mean HHRs (0.510 and 0.533) primarily due to lower baseline thermal conditions (Yuhang's mean LST: 0.798) and highly dispersed populations. However, these peripheral areas face distinct infrastructural deficits, evidenced by average distances to medical facilities exceeding 1,300 m, presenting a different typology of spatial health vulnerability.

3.5.2 Medical Resource Allocation Efficiency and Identification of the "Central Paradox"

Through a bivariate spatial coupling analysis of district-level medical resource density against the HHR and elderly population distribution (Fig. 11), this study identifies a counter-intuitive spatial configuration termed the "central paradox." The data reveal that selected urban districts exhibit a compounding effect where maximum medical supply directly overlaps with the highest demographic and environmental vulnerability. Specifically, Gongshu and Shangcheng districts demonstrate the highest mean medical resource densities (0.176 and 0.152, respectively). However, rather than mitigating risk, these districts simultaneously record the most severe heat risk profiles (HHRs of 0.590 and 0.558) and the heaviest burdens of elderly population (normalized means

of 0.187 and 0.152). This spatial alignment suggests that the physical advantage of geographic proximity to healthcare in the urban core is functionally neutralized by extreme vulnerability concentration, resulting in sustained high-risk statuses despite dense infrastructure.

Conversely, peripheral and transitioning districts exhibit a pronounced spatial mismatch characterized by elevated environmental risk coupled with deficient medical infrastructure. Linping District presents the most critical deviation: while ranking third in overall heat risk (HHR of 0.541), its medical resource density is starkly constrained at 0.038, exposing a significant supply–demand deficit. This pattern of high thermal exposure paired with acute medical scarcity is further replicated in adjacent expanding districts, notably Xiaoshan (HHR = 0.519, medical resource density = 0.019) and Qiantang (HHR = 0.517, medical resource density = 0.017). Even districts like Xihu and Yuhang maintain relatively high risk levels (HHRs of 0.502 and 0.490) while possessing limited medical resource density (0.042 and 0.011) relative to the urban core.

In contrast, districts such as Binjiang exhibit the lowest heat risk profile in the study area (HHR = 0.428) while maintaining a moderate-to-high medical resource density (0.084), indicating a more resilient supply–demand balance. Ultimately, the bivariate assessment isolates two primary trajectories of spatial inequity: the "high medical–high vulnerability" paradox in the historic urban core (e.g., Gongshu, Shangcheng) and the critical "high risk–low medical" mismatch in peripheral zones (e.g., Linping, Xiaoshan, Qiantang). These findings challenge traditional density-based planning assumptions and establish clear spatial priorities for targeted, equitable public health infrastructure interventions.

3.5.3 Amplification Effects and Nonlinear Association of Street Canyon Morphology on Heat Risk

In exploring the physical drivers of heat risk, a prominent, albeit non-linear, positive association is observed between street network density and the HHR (Fig. 12-1). As street density deciles increase from the 1st to the 9th, the mean HHR scales steadily from 0.495 to a peak of 0.567, accompanied by a corresponding rise in median values (0.484 to 0.566). This trajectory indicates that denser street canyon morphologies are generally coupled with more severe heat accumulation, driven by the UHI effect. Morphologically, overly dense structural forms obstruct natural ventilation corridors and significantly increase the proportion of impervious surfaces, thereby hindering thermal dissipation. Interestingly, a slight inversion occurs at the extreme high-density end (10th decile), where the mean HHR marginally recedes to 0.553. This non-linear inflection suggests a threshold where specific high-density morphologies may begin to provide localized shading, partially offsetting thermal exposure.

The district-level bivariate analysis (Fig. 12-2) further delineates this morphological impact by categorizing distinct spatial typologies. Traditional central districts such as Gongshu (street density: 0.349; HHR: 0.604) and Shangcheng (street density: 0.356; HHR: 0.569) epitomize "high-density high-risk agglomerations," validating the broader trend. Conversely, the data reveal critical spatial anomalies, most notably in Binjiang District. Despite registering the highest overall average street density in the study area (0.371), Binjiang maintains the lowest composite heat risk (HHR: 0.442).

This divergence represents a macro-level manifestation of "high-density but low-risk" zones, or potential "cold canyons." The existence of such areas provides vital urban design insights:

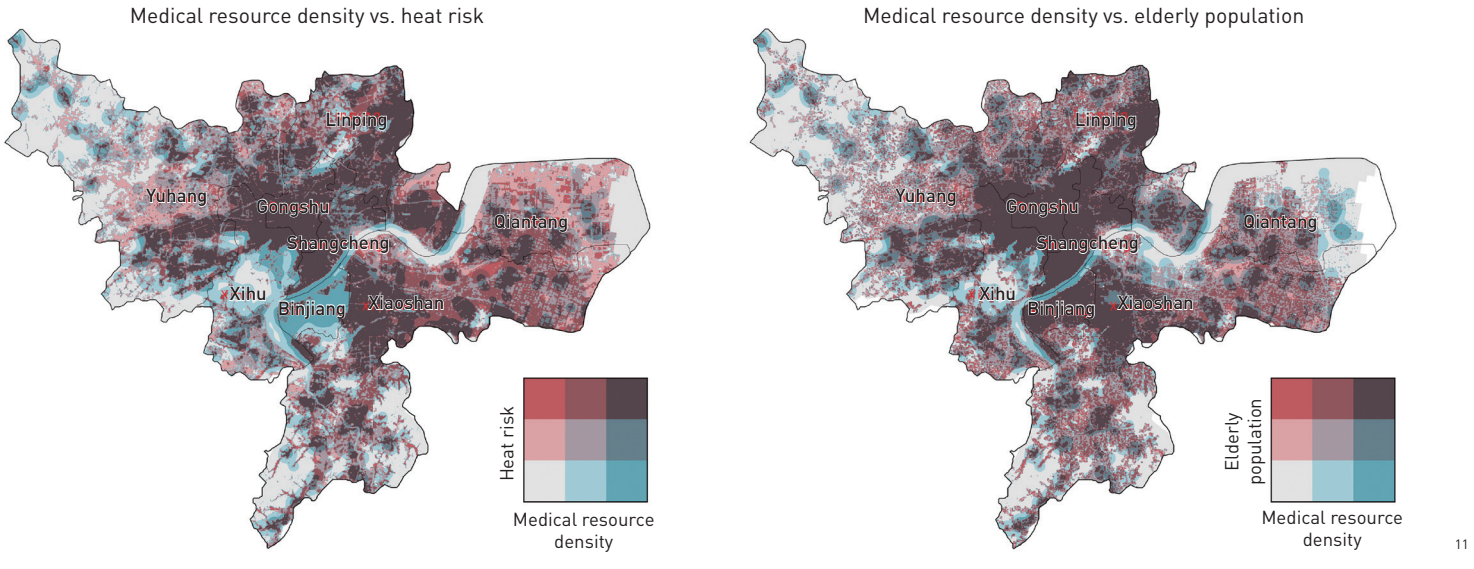

Fig. 11 Medical resources allocation assessment of the selected urban districts of Hangzhou.

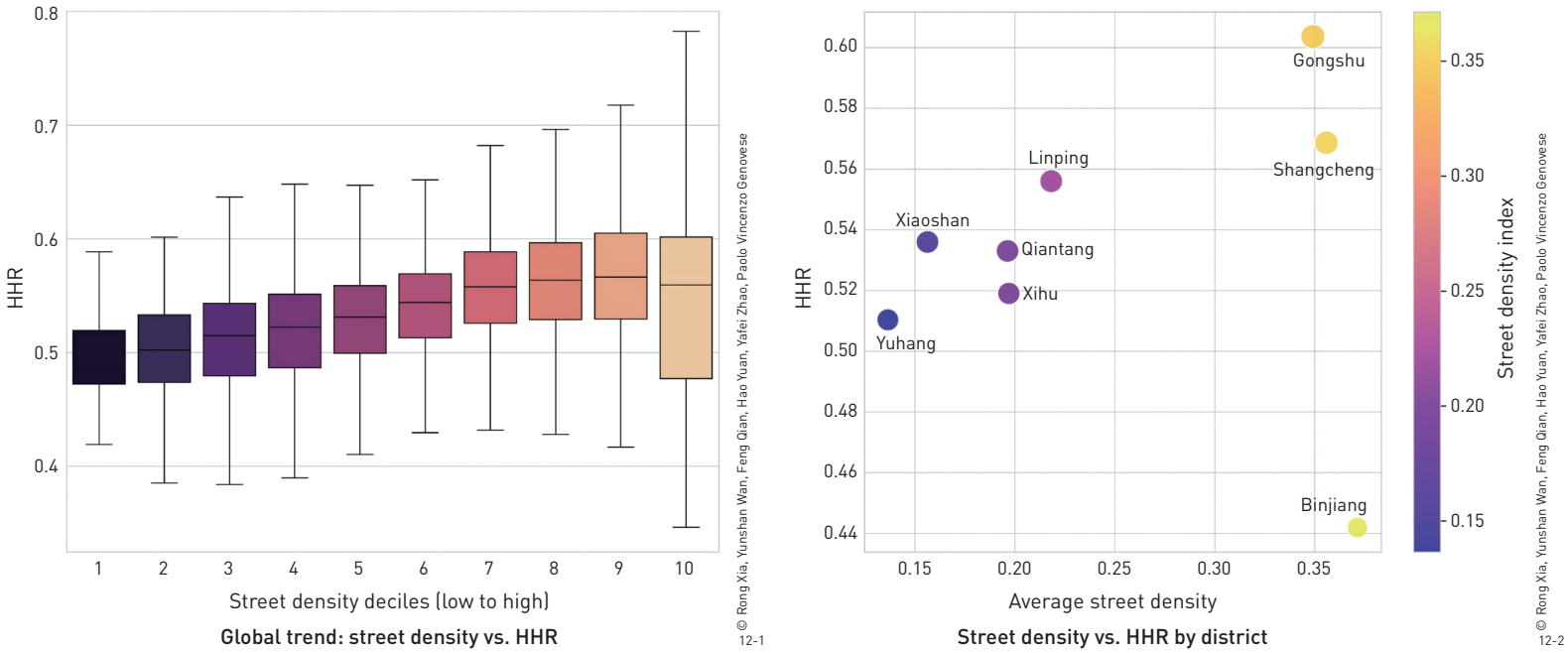

Fig. 12 Relationship between street network density and HHR across selected urban districts.

it demonstrates that high construction and street intensity can be decoupled from severe heat risk. These zones likely benefit from a combination of lower baseline demographic vulnerability and optimized physical parameters—such as specific aspect ratios (height-to-width) for deep shading, high-quality street tree canopy coverage, and optimized ventilation orientations. This evidence confirms that optimizing morphological parameters can effectively mitigate the negative environmental impacts of urban densification, offering an empirical blueprint for the micro-regeneration of highly vulnerable urban environments.

4 Conclusions and Policy Suggestions

4.1 Conclusions

This study systematically quantifies the triadic coupling between land use, carbon emissions, and heat-related health risks in the Hangzhou metropolitan area. The findings reveal that while the overall HRI is moderate, it exhibits a significant "old city–new district" dualism and a counter-intuitive "accessibility paradox."

Firstly, spatial heterogeneity is driven by the overlap of thermal hazards and demographic vulnerability. In the aging urban cores of Gongshu and Shangcheng, the HRI is maximized (reaching 0.590 and 0.558, respectively) due to the high weight of the elderly ratio (0.8667) and the heat-trapping effect of high-density "street canyons." Conversely, newer districts like Binjiang maintain lower risks despite high surface temperatures, owing to a younger demographic structure. This proves that urban heat health is not merely a climate issue but a socio-spatial inequality issue mediated by land use.

Secondly, the study identifies a "service pressure redundancy" in the urban center. Despite having the shortest physical distance to medical facilities (approximately 305 m), the high population density in core areas dilutes per capita resources, leading to high-risk congestion. In contrast, Linping District represents a "resource gap" zone, where over 55% of the area faces high heat risk but lacks sufficient medical and cooling infrastructure.

Finally, LUCC acts as the decisive mediator between carbon and heat. The projected expansion of 6,005.74 hm^2 of construction land by 2030, predominantly at the expense of forests and arable land, will not only increase net carbon emissions by 549,992.86 tC/yr but also erode the "cold island" buffers essential for public health. These findings emphasize that landscape-led interventions must prioritize the synergy between carbon sequestration and thermal regulation to achieve the WHO's Healthy City objectives.

4.2 Policy Suggestions for Building a Resilient Hangzhou

To translate these findings into actionable urban regeneration, Hangzhou should transition from "resource expansion" to "spatial-targeted precision intervention." We propose a categorized strategy based on the identified risk profiles.

4.2.1 Core Areas: Micro-Climate Adaptation and Stock Optimization

For these "high-medical/high-risk" zones (e.g., Gongshu, Shangcheng) where large-scale demolition is unfeasible, policies

should mandate micro-scale landscape interventions to break the "high-density/high-risk" cycle. Implement "cold canyon" morphology optimization in street-level micro-updates. This includes increasing the aspect ratio of street shading, deploying vertical greening on building envelopes, and installing pocket parks with high-transpiration native canopy trees in order to reduce localized thermal exposure and alleviate service pressure on existing medical hubs during extreme heatwaves.

4.2.2 Edge High-Risk Zones: Spatial Repair and Decentralized Health Buffers

For these "low-medical/high-risk" areas (e.g., Linping), the priority is to bridge the equity gap in health infrastructure. Instead of building large centralized hospitals, policy should incentivize the "decentralized embedding" of community health service units and "cooling centers" within 15-minute walking circles of high-vulnerability clusters. These facilities should be integrated with GBIs (e.g., permeable community gardens) to serve as both social spaces and emergency thermal shelters in order to achieve "service opportunity equality" rather than mere "physical proximity."

4.2.3 Northwest Ecological Basins: Source Protection and Growth Control

For these "low-medical/low-risk" zones (e.g., Yuhang, Qiantang), the focus is on preserving the city's regional cooling capacity. Establish a "climate-ecological redline" to prevent urban sprawl from encroaching on carbon-sequestering forests and water bodies. Land-use transitions must be strictly regulated to maintain the connectivity of natural cold-source corridors that ventilate the urban core in order to maintain the existing 19.41% low-risk base as a permanent carbon sink and thermal buffer.

4.2.4 Integrated Governance: HRI-Informed Planning Framework

Hangzhou should pioneer an "integrated heat-health dashboard" as a regulatory tool. Future land-use permits should undergo a "thermal impact assessment," and the HRI should be used to dynamically allocate public health funding. By embedding health equity and carbon neutrality into the legal framework of urban planning, Hangzhou can transition from a growth-oriented metropolis to a thriving, low-carbon Healthy City ecosystem.

Competing interests | The authors declare that they have no competing interests.

REFERENCES

[1] Grimm, N. B., Faeth, S. H., Golubiewski, N. E., Redman, C. L., Wu, J., Bai, X., & Briggs, J. M. (2008). Global change and the ecology of cities. *Science*, *319*(5864), 756–760.

[2] Foley, J. A., DeFries, R., Asner, G. P., Barford, C., Bonan, G., Carpenter, S. R., ... Snyder, P. K. (2005). Global consequences of land use. *Science*, *309*(5734), 570–574.

[3] Kalnay, E., & Cai, M. (2003). Impact of urbanization and land-use change on climate. *Nature*, *423*(6939), 528–531.

[4] Wen, J., Chuai, X., Zuo, T., Cai, H., Cai, L., Zhao, R., & Chen, Y. (2023). Land use change on the surface area and the influence on carbon, *Ecological Indicators*, *153*, 110400.

[5] Zhao, L., Lee, X., Smith, R. B., & Oleson, K. (2014). Strong contributions of local background climate to urban heat islands. *Nature*, *511*(7508), 216–219.

[6] Weng, Q., Lu, D., & Schubring, J. (2004). Estimation of land surface temperature–vegetation abundance relationship for urban heat island studies. *Remote Sensing of Environment*, *89*(4), 467–483.

[7] Watts, N., Amann, M., Arnell, N., Ayeb-Karlsson, S., Belesova, K., Boykoff, M., ... & Montgomery, H. (2019). The 2019 report of The Lancet Countdown on health and climate change: ensuring that the health of a child born today is not defined by a changing climate. *The Lancet*, *394*(10211), 1836–1878.

[8] Mora, C., Dousset, B., Caldwell, I. R., Powell, F. E., Geronimo, R. C., Bielecki, C. R., ... & Trauernicht, C. (2017). Global risk of deadly heat. *Nature Climate Change*, *7*(7), 501–506.

[9] Rydin, Y., Bleahu, A., Davies, M., Dávila, J. D., Friel, S., De Grandis, G., ... Wilson, J. (2012). Shaping cities for health: Complexity and the planning of urban environments in the 21st century. *The Lancet*, *379*(9831), 2079–2108.

[10] Zheng, H. W., Shen, G. Q., & Wang, H. (2014). A review of recent studies on sustainable urban renewal. *Habitat International*, *41*, 272–279.

[11] Liu, Y., Sang, M., Xu, X., Shen, L., & Bao, H. (2023). How can urban regeneration reduce carbon emissions? A bibliometric review. *Land*, *12*(7), 1328.

[12] Joshi, K., Khan, A., Anand, P., & Sen, J. (2024). Understanding the synergy between heat waves and the built environment: a three-decade systematic review informing policies for mitigating urban heat island in cities. *Sustainable Earth Reviews*, *7*, 25.

[13] Fu, Q., Zheng, Z., Sarker, M. N. I., & Lv, Y. (2024). Combating urban heat: Systematic review of urban resilience and adaptation strategies. *Heliyon*, *10*(17), e37001.

[14] Tzoulas, K., Korpela, K., Venn, S., Yli-Pelkonen, V., Kaźmierczak, A., Niemela, J., & James, P. (2007). Promoting ecosystem and human health in urban areas using Green Infrastructure: A literature review. *Landscape and Urban Planning*, *81*(3), 167–178.

[15] Ramaswami, A., Pandey, B., Li, Q., Das, K., & Nagpure, A. (2023). Toward zero-carbon urban transitions with health, climate resilience, and equity co-benefits: Assessing nexus linkages. *Annual Review of Environment and Resources*, *48*, 81–121.

[16] Clarke, K. C., Hoppen, S., & Gaydos, L. (1997). A self-modifying cellular automaton model of historical urbanization in the San Francisco Bay Area. *Environment and Planning B: Planning and Design*, *24*(2), 247–261.

[17] Muller, M. R., & Middleton, J. (1994). A Markov model of land-use change dynamics in the Niagara Region, Ontario, Canada. *Landscape Ecology*, *9*, 151–157.

[18] Pontius, G. R., & Malanson, J. (2005). Comparison of the structure and accuracy of two land change models. *International Journal of Geographical Information Science*, *19*(2), 243–265.

[19] Liang, X., Guan, Q., Clarke, K. C., Liu, S., Wang, B., & Yao, Y. (2021). Understanding the drivers of sustainable land expansion using a patch-generating land use simulation (PLUS) model: A case study in Wuhan, China. *Computers, Environment and Urban Systems*, *85*, 101569.

[20] Hu, X., Zhu, W., Shen, X., Bai, R., Shi, Y., Li, C., & Zhao, L. (2024). Exploring the predictive ability of the CA–Markov model for urban functional area in Nanjing old city. *Scientific Reports*, *14*, 18453.

[21] Liu, X., Liang, X., Li, X., Xu, X., Ou, J., Chen, Y., … Pei, F. (2017). A future land use simulation model (FLUS) for simulating multiple land use scenarios by coupling human and natural effects. *Landscape and Urban Planning*, *168*, 94-116.

[22] Verburg, P. H., Alexander, P., Evans, T., Magliocca, N. R., Malek, Z., Rounsevell, M. D. A., & van Vliet, J. (2019). Beyond land cover change: towards a new generation of land use models. *Current Opinion in Environmental Sustainability*, *38*, 77–85.

[23] IPCC. (2022). *Climate change 2022: Impacts, adaptation, and vulnerability*.

[24] Li, F., Yigitcanlar, T., Li, W., Nepal, M., Nguyen, K., & Dur, F. (2024). Understanding urban heat vulnerability: Scientometric analysis of five decades of research. *Urban Climate*, *56*, 102035.

[25] Xu, T., Gong, J., Cao, J., Tian, Y., Rao, Y., Ma, Y., … Kerimbaevich, E. F. (2025). Differential spatiotemporal patterns in urban thermal environment driven by impervious surface trajectories: A multi-scale assessment framework. *Environmental Impact Assessment Review*, *117*, 108178.

[26] Ahmed, A. N., AlDahoul, N., Aziz, N. A., Huang, Y. F., Sherif, M., & El-Shafie, A. (2025). The urban heat Island effect: A review on predictive approaches using artificial intelligence models. *City and Environment Interactions*, *28*, 100234.

[27] Li, B., Liang, S., Liu, X., Ma, H., Chen, Y., Liang, T., & He, T. (2021). Estimation of all-sky 1 km land surface temperature over the conterminous United States. *Remote Sensing of Environment*, *266*, 112707.

[28] Zhou, D., Zhao, S., Liu, S., Zhang, L., & Zhu, C. (2014). Surface urban heat island in China's 32 major cities: Spatial patterns and drivers. *Remote Sensing of Environment*, *152*, 51–61.

[29] Lundberg, S. M., Erion, G., Chen, H., DeGrave, A., Prutkin, J. M., Nair, B., … Lee, S. I. (2020). From local explanations to global understanding with explainable AI for trees. *Nature Machine Intelligence*, *2*, 56–67.

[30] Grimm, N., Redman, C., Boone, C., Childers, D., Harlan, S., & Turner, B. (2013). Viewing the Urban Socio-Ecological System Through a sustainability Lens: Lessons and Prospects From the Central Arizona–Phoenix LTER Programme. In: S. Singh, H. Haberl, M. Chertow, M. Mirtl, & M. Schmid (Eds.), *Long Term Socio-Ecological Research: Studies in Society-Nature Interactions Across Spatial and Temporal Scales* (pp. 217–246). Springer.

[31] Lee, K. O., Mai, K. M., & Park, S. (2023). Green space accessibility helps buffer declined mental health during the COVID-19 pandemic: evidence from big data in the United Kingdom. *Nature Mental Health*, *1*, 124–134.

[32] Zhang, X., & Zhang, D. (2023). Urban carbon emission scenario prediction and multi-objective land use optimization strategy under carbon emission constraints. *Journal of Cleaner Production*, *430*, 139684.

[33] Kang, J., Zhang, B., & Dang, A. (2024). A novel geospatial machine learning approach to quantify non-linear effects of land use/land cover change (LULCC) on carbon dynamics. *International Journal of Applied Earth Observation and Geoinformation*, *128*, 103712.

[34] Fernandes, M. M., Fernandes, M. R. M., Garcia, J. R., Matricardi, E. A. T., Lima, A. H. S., Araújo Filho, R. … Cunha Filho, M. (2021). Land use and land cover changes and carbon stock valuation in the São Francisco river basin, Brazil. *Environmental Challenges*, *5*, 100247.

[35] Güneralp, B., Zhou, Y., Ürge-Vorsatz, D., Gupta, M., Yu, S., Patel, P. L., … Seto, K. C. (2017). Global scenarios of urban density and its impacts on building energy use through 2050. *PNAS*, *114*(34), 8945–8950.

[36] Dai, Q., Liu, X., Sun, F., & Ren, F. (2024). Ensemble intelligence prediction algorithms and land use scenarios to measure carbon emissions of the Yangtze River Delta: A machine learning model based on Long Short-Term Memory. *PLoS ONE*, *19*(12), e0311441.

[37] Rogelj, J., den Elzen, M., Höhne, N., Fransen, T., Fekete, H., Winkler, H., … Meinshausen, M. (2016). Paris Agreement climate proposals need a boost to keep warming well below 2 °C. *Nature*, *534*, 631–639.

[38] Wu, J., Liu, C., Guo, H., Li, P., & Sun, W. (2024). Examining intra-city carbon budget and carbon balance zoning based on firm-level big data: A case study of Nanjing, China. *Ecological Indicators*, *166*, 112304.

[39] IPCC. (2014). *Climate Change 2014: Impacts, Adaptation, and Vulnerability*. Cambridge University Press.

[40] Cai, B., Zhu, S., Yu, S., Dong, H., Zhang, C., Wang, C., … Zheng, X. (2019). The interpretation of 2019 refinement to the 2006 IPCC guidelines for national greenhouse gas inventory. *Environmental Engineering*, *37*(8), 1–11.

[41] Lai, L. (2010). *Carbon emission effect of land use in China [Doctoral dissertation]*. Nanjing University.

[42] Ru, K. (2020). *Carbon emission and county-level carbon compensation of Fujian Province based on land use [Master's thesis]*. Fujian Agriculture and Forestry University.

[43] Arnfield, A.J. (2003). Two decades of urban climate research: a review of turbulence, exchanges of energy and water, and the urban heat island. *International Journal of Climatology*, *23*(1), 1–26.

[44] Li, X., Zhou, Y., Yu, S., Jia, G., Li, H., & Li, W. (2019). Urban heat island impacts on building energy consumption: A review of approaches and findings. *Energy*, *174*, 407–419.

LAF | https://doi.org/10.15302/J-LAF-2026-0046
第14卷 / 第6期 / 260046 / 2026
收稿日期 | 2025-09-27　录用日期 | 2026-04-28
中图分类号 | TU986　文献标识码 | A

基于健康公平视角的土地利用与碳–热风险耦合机制研究

夏荣[1,2]，万芸杉[2,3]，钱锋[3]，原昊[3]，赵亚飞[2,4]，罗杰威[2,3,*]

1 浙江农林大学风景园林与建筑学院，杭州 311300
2 浙江大学建筑历史与遗产保护国际中心，杭州 310058
3 浙江大学建筑工程学院，杭州 310058
4 青岛黄海学院智慧城市工程学院，青岛 266427

***通信作者**
地址：杭州市西湖区余杭塘路866号
邮编：310058
邮箱：pavic@zju.edu.cn

摘要

城市土地利用转型也重塑了区域碳循环过程和热环境格局，但土地利用变化、碳排放与城市热相关健康风险之间的耦合作用机制仍有待系统探究。本研究以中国杭州市区部分地区为研究区域，构建了一个基于融合多种预测模型的智能集成框架：通过融合土地利用集成预测、土地利用碳排放（Land Use Carbon Emissions，LUCE）核算、热健康风险评估，以及空间公平性分析，定量揭示土地利用变化、碳排放与热健康风险之间的相互作用关系。研究利用该框架对2025—2030年未来土地利用变化趋势进行模拟，计算LUCE和热健康风险，以评估环境风险和社会脆弱性。

研究结果表明，热–碳耦合系统具有显著的空间异质性。建设用地扩张是未来LUCE增长的主要驱动因素，预计到2030年，由于森林和耕地向建设用地转化，区域碳排放将增加。同时，热健康风险呈现明显的“老城区–新城区”空间分异特征。尽管城市核心区域具有较高的医疗资源可达性，但高人口压力导致潜在的医疗服务供需错配；相比之下，临平等外围区域由于医疗服务和降温基础设施不足而面临较高风险。城市形态分析进一步表明，街道密度与热风险之间存在非线性关系，凸显了气候适应型城市设计的重要性。

总体而言，本研究表明土地利用变化是连接碳排放与热健康风险的重要中介机制。未来城市韧性提升策略应突破传统基础设施扩张模式，转向空间精准化干预，包括保护生态降温廊道、优化高密度城市空间形态以及公平配置热适应资源。本研究构建的综合分析框架可为快速城市化地区开展气候韧性和健康导向型城市规划提供定量依据。

关键词

健康城市；城市热暴露；土地利用变化；碳排放；气候–健康耦合关系

文章亮点

- 构建了一个连接土地利用变化、碳排放和热健康风险的综合分析框架
- 利用智能集成模型预测未来土地利用变化趋势，提高了LUCC模拟的稳定性和可靠性
- 揭示了建设用地扩张驱动碳排放增加、削弱区域生态降温能力的作用机制
- 识别了老龄化城市核心区与新兴外围区域之间显著的热健康风险空间差异
- 阐明了城市空间形态和生态缓冲系统在缓解未来热相关风险中的重要作用

基金项目

- 浙江大学求是特聘教授科研启动基金项目（编号：113000+1944224R1/005）
- 安徽省重点实验室开放课题（编号：513101-W02401）